

Restraining Oxygen Release and Suppressing Structure Distortion in Single-Crystal Li-Rich Layered Cathode Materials

Jianming Sun, Chuanchao Sheng, Xin Cao,* Pengfei Wang, Ping He,* Huijun Yang, Zhi Chang, Xiyan Yue, and Haoshen Zhou*

Li-rich oxides can be regarded as the next-generation cathode materials for high-energy-density Li-ion batteries since additional oxygen redox activities greatly increase output energy density. However, the oxygen loss and structural distortion induce low initial coulombic efficiency and severe decay of cycle performance, further hindering their industrial applications. Herein, the representative layered Li-rich cathode material, $\text{Li}_{1.2}\text{Ni}_{0.2}\text{Mn}_{0.6}\text{O}_2$, is endowed with novel single-crystal morphology. In comparison to its polycrystal counterpart, not only can serious oxygen release be effectively restrained during the first oxygen activation process, but also the layered/spinel phase transition can be well suppressed upon cycling. Moreover, the single-crystal cathode exhibits the limited volume change and persistent presence of superlattice peaks upon Li^+ (de)intercalation processes, resulting in enhanced structural stability with absence of crack generation and successive utilization of oxygen redox reaction during long-term cycling. Benefiting from these unique features, the single-crystal Li-rich electrode not only yields a high reversible capacity of 257 mAh g^{-1} , but also achieves excellent cycling performance with 92% capacity retention after 200 cycles. These findings demonstrate that the morphology design of single crystals can be regarded as an effective strategy to realize high-energy density and long-life Li-ion batteries.

based on cationic redox reactions.^[2] However, the Li-rich oxides always suffer from the serious oxygen release, which induces the irreversible capacity and low columbic efficiency during the initial cycles, further hindering their practical applications.^[3] Meanwhile, the irreversible lattice oxygen loss would inevitably accelerate the structural distortion, which causes the unfavorable layered to spinel phase transition upon cycling, resulting in serious voltage fade and capacity deterioration. More importantly, most Li-rich layered cathode materials generally possess polycrystal morphology, which would exacerbate the side reactions between cathode and electrolyte, crack generation, and violent volume change, severely destroying the structural stability and cycle performances during long-term cycling.^[4–6]

Tesla company and Dahn group jointly launched a Million-Mile Battery plan by employment of single-crystal $\text{LiNi}_{0.5}\text{Mn}_{0.3}\text{Co}_{0.5}\text{O}_2$ cathode material, which has excellent capacity retention during long-term cycling.^[7] The pouch cell with single-crystal $\text{LiNi}_{0.5}\text{Mn}_{0.3}\text{Co}_{0.5}\text{O}_2$ cathode and artificial graphite anode delivered the remarkable 92% capacity retention after 4700 cycles. In contrast, the polycrystal layered Ni-rich cathode materials generally displayed the rapid capacity decay especially at high voltage and high temperature during long-term cycling because of the serious crack generation triggered by the accumulation of heterogeneous stress.^[8] Furthermore, the anode side also

1. Introduction


To satisfy the high standards of next-generation Li-ion batteries, the development of high-energy-density cathode materials has been the top priority.^[1] Li-rich cathode materials generally can achieve the high output capacity of beyond 250 mAh g^{-1} by coupling with anionic redox activities, which greatly breaks through the capacity limitation of traditional cathode materials

J. Sun, X. Cao, H. Yang, Z. Chang, H. Zhou
Energy Technology Research Institute
National Institute of Advanced Industrial Science and Technology (AIST)
1-1-1, Umezono, Tsukuba 305–8568, Japan
E-mail: cao.xin@aist.go.jp; hszhou@nju.edu.cn

J. Sun, X. Cao, H. Zhou
Graduate School of System and Information Engineering
University of Tsukuba
1-1-1, Tennoudai, Tsukuba 305–8573, Japan

C. Sheng, P. Wang, P. He, H. Zhou
Center of Energy Storage Materials & Technology
College of Engineering and Applied Sciences
Jiangsu Key Laboratory of Artificial Functional Materials
National Laboratory of Solid State Microstructures
and Collaborative Innovation Center of Advanced Microstructures
Nanjing University
Nanjing 210093, P. R. China
E-mail: pinghe@nju.edu.cn

X. Yue
Graduate School of Science and Technology
Hirosaki University
1-Bunkyocho, Hirosaki 036–8560, Japan

 The ORCID identification number(s) for the author(s) of this article can be found under <https://doi.org/10.1002/adfm.202110295>.

DOI: 10.1002/adfm.202110295

suffered from the transition metal (TM) reduction reaction on the surface, which can be attributed to the TM dissolution from polycrystal cathode side, further accelerating the cycling performance fade of pouch cells.^[7a,8,9] Therefore, the design of single-crystal morphology can be regarded as an effective strategy to improve the structural stability and electrochemical performances by means of unique features, including crack-free, restrained side reactions, and limited gas generations, homogeneous internal stress, etc. Besides, the single-crystal morphology is beneficial for surface modifications such as surface doping and coating in comparison with polycrystal counterparts,^[10] which has the breathtaking potentiality to optimize the electrochemical performances of cathode materials in future studies. Although the current polycrystal Li-rich materials have realized the relatively high output capacity, the structural stability and cycle performance should be further improved.^[11] Therefore, the design of single-crystal morphology is expected to resolve the intrinsic problems of Li-rich materials including the oxygen release and structural distortion upon cycling.

Herein, we developed the single-crystal Li-rich $\text{Li}_{1.2}\text{Ni}_{0.2}\text{Mn}_{0.6}\text{O}_2$ (SC-LLNMO) as cathode material, in which the oxygen-related plateau located at 4.75 V during the first charging process, different from that of typical polycrystal $\text{Li}_{1.2}\text{Ni}_{0.2}\text{Mn}_{0.6}\text{O}_2$ (PC-LLNMO, at 4.55 V). The PC-LLNMO displayed serious oxygen release upon the first oxygen activation process, resulting in irreversible capacity of 101 mAh g^{-1} during discharging, whereas the irreversible oxygen behavior can be well restrained in SC-LLNMO. Moreover, the layered/spinel phase transition can be effectively suppressed in SC sample, boosting the structural stability and harvesting the limited voltage decay upon long cycling. Notably, SC-LLNMO sample exhibited limited volume change (1.47%) upon Li^+ (de)

intercalation processes in contrast with PC-LLNMO (2.34%), where the serious crack generation only can be detected in PC electrode. Benefiting from the restrained oxygen loss, limited volume change, and stable structure evolution, SC-LLNMO achieved the superior cycling performance with capacity retention of 92% after 200 cycles), whereas PC counterpart presented the rapid capacity decay with 68% capacity retention at same electrochemical conditions.

2. Results and Discussion

For comparison, PC-LLNMO was first synthesized by traditional solid-state reaction, which displayed the typical morphology of spherical secondary particle with $5 \mu\text{m}$ diameter, constructed by primary nanoparticles with diameter distribution from 100 to 200 nm, shown in scanning electron microscope (SEM) and transmission electron microscope (TEM) images (Figure 1a, inset). According to the Rietveld refinement of X-ray powder diffraction (XRD) pattern, the Li-rich PC-LLNMO sample can be indexed the structure with two space groups of hexagonal R-3m and monoclinic C2/m space groups (Figure 1a).^[12] The XRD patterns were calculated by General Structure Analysis System (GSAS) with excellent fitting result parameters of $\chi^2 = 1.47$ and $R_{\text{wp}} = 2.97\%$.^[13] The detailed results of lattice parameters were shown in Table S1, Supporting Information. SC-LLNMO was successfully synthesized by co-precipitation assisted molten salt strategy, which displayed the octahedral morphology with single primary particles with large diameter distribution from 300 to 600 nm (Figure 1b, inset). Furthermore, the Rietveld refinement results of XRD pattern proved that SC-LLNMO also possessed two characteristics of layered hexagonal R-3m

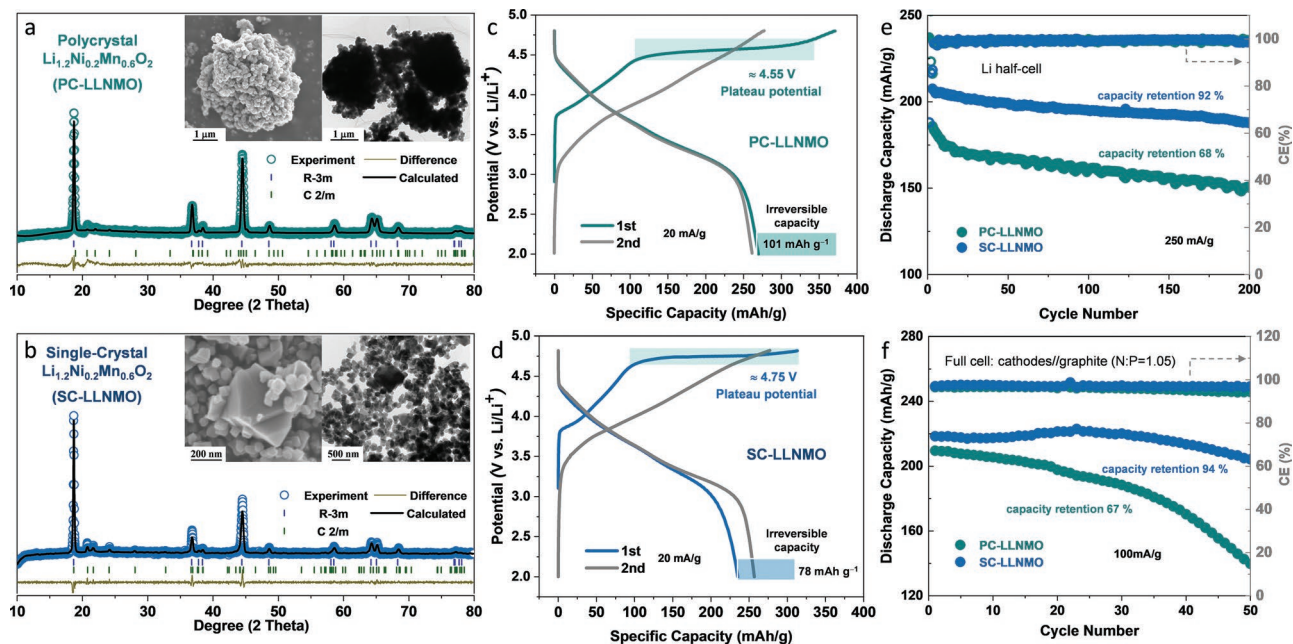


Figure 1. Structural characterizations and electrochemical performances of PC- and SC-LLNMO. The XRD patterns and corresponding Rietveld refinement results of a) PC- and b) SC-LLNMO. The corresponding TEM and SEM images are shown in the inset. The typical charge and discharge profiles of c) PC- and d) SC-LLNMO electrodes during initial two cycles between 2 and 4.8 V at the current density of 20 mA g^{-1} . Cycling performances of PC- and SC-LLNMO electrodes in e) Li half-cells and f) full cells with graphite anode.

and monoclinic C2/m space groups, which provided the excellent fitting results of $\chi^2 = 1.91$ and $R_{wp} = 5.16\%$. The lattice parameters of SC sample also can be observed in Table S1, Supporting Information. In addition, Energy Dispersive Spectroscopy (EDS) mapping indicated that involved Ni, Mn, O elements uniformly distributed in the PC and SC samples (Figure S1, Supporting Information). Besides, the Inductively Coupled Plasma (ICP) confirmed the element ratios of both two samples, in agreement with the designed chemical formula of $\text{Li}_{1.2}\text{Ni}_{0.2}\text{Mn}_{0.6}\text{O}_2$ (Table S2, Supporting Information).

The electrochemical behaviors of PC- and SC-LLNMO were investigated in Li half-cells between ≈ 2.0 and 4.8 V (vs Li/Li⁺) at 20 mA g⁻¹. Upon the first charging process, PC sample displayed the combination of a slope region and a plateau at 4.55 V, which generally can be identified as the TM-based and oxygen oxidation activities, in agreement with previous works of Li-rich $\text{Li}_{1.2}\text{Ni}_{0.2}\text{Mn}_{0.6}\text{O}_2$ with polycrystal morphology.^[14] During the subsequent discharging process, PC electrode suffered from the serious irreversible capacity of 101 mAh g⁻¹ ($\approx 27.4\%$ of charge capacity), which is mainly caused by lattice oxygen loss upon charging process since oxygen molecular generated upon charge is difficult to be well reduced to lattice oxygen during discharge. In contrast, during the initial oxygen activation process, the location of oxygen-related plateau within SC-LLNMO reached to 4.75 V, which is totally different from all previous Li-rich cathode materials such as Li_2MnO_3 and $x\text{Li}_2\text{MnO}_3 \cdot (1-x)\text{LiTMO}_2$ (TM = Mn, Ni, and Co), indicating relatively strong electrochemical driving force is required to realize oxygen activation in SC-LLNMO. Moreover, the SC-LLNMO electrode exhibited the limited irreversible capacity of 78 mAh g⁻¹ ($\approx 25.3\%$ of charge capacity) during the first cycle, which is in stark contrast with serious capacity loss within PC-LLNMO, suggesting more stable oxygen redox reactions can be achieved within SC electrode. Therefore, it is rational to deduce that the design for single-crystal morphology is beneficial for restraining the irreversible oxygen release, further boosting the structural stability and electrochemical performances during long-term cycling. In addition, SC-LLNMO realized the high reversible discharge capacity of 257 mAh g⁻¹ during the second cycle.

Furthermore, the rate performances of both PC- and SC-LLNMO were further investigated at the current density of 20 , 50 , 100 , 200 mA g⁻¹, respectively (Figures S2 and S3, Supporting Information). Intriguingly, SC sample showed the

superior rate performance at both low and high current density, which is totally different from rate results in previous studies.^[15a] Therefore, the galvanostatic intermittent titration technique tests were performed to calculate Li⁺ diffusion coefficient (D_{Li^+}) and study the kinetics behaviors of both PC-LLNMO and SC-LLNMO electrodes (Figure S4, Supporting Information),^[15b,c] in which SC sample harvested the higher D_{Li^+} values in both TM-based and oxygen-related regions. It proved the superior rate performances can be obtained within SC sample during both charging and discharging processes compared with PC sample. Besides, the remarkably high output capacity of 197 mAh g⁻¹ can be obtained within SC sample at high current density of 200 mA g⁻¹, which is higher than most Li-rich cathode materials with polycrystal morphology.^[15d,e]

Notably, SC-LLNMO also exhibited excellent long-term cycle performances in both Li half-cells and full-cells (Figure 1e,f). At the current density of 250 mA g⁻¹, the limited capacity loss (0.04% per cycle) and excellent retention rate (92%) within the SC-LLNMO after 200 cycles, whereas the PC sample displayed the serious capacity loss (0.16%) with poor capacity retention rate (68%). At low current density of 25 mA g⁻¹, the output capacity of SC-LLNMO reached to 263 mAh g⁻¹ even after 50 cycles, while PC sample lost almost 20 mAh g⁻¹ capacity at the same electrochemical condition (Figure S5a, Supporting Information). Besides, the serious voltage decay can be well restrained in the SC sample, whereas the PC sample exhibited serious voltage fade of 0.257 V after 50 cycles, indicating the excellent layered structure can be well maintained in SC-LLNMO, but PC-LLNMO suffered from the severe layered/spinel phase transition (Figure S5b, Supporting Information). To meet the high standards of practical applications in battery industries, the full cells with Li-rich cathodes and graphite anode were assembled, in which the PC and SC samples displayed the capacity retention of 67% and 94% , respectively (Figure 1f), suggesting the single-crystal Li-rich oxides are promising high-energy-density cathode materials for next-generation Li-ion batteries.

The in situ gas chromatography–mass spectrometry (GC-MS) measurements were conducted to detect irreversible oxygen redox activities for both PC- and SC-LLNMO samples during initial two cycles (Figure 2, Figures S6 and S7, Supporting Information). The low-volatility alkyl carbonate electrolyte (1 M LiPF₆ in PC electrolyte) was employed to in

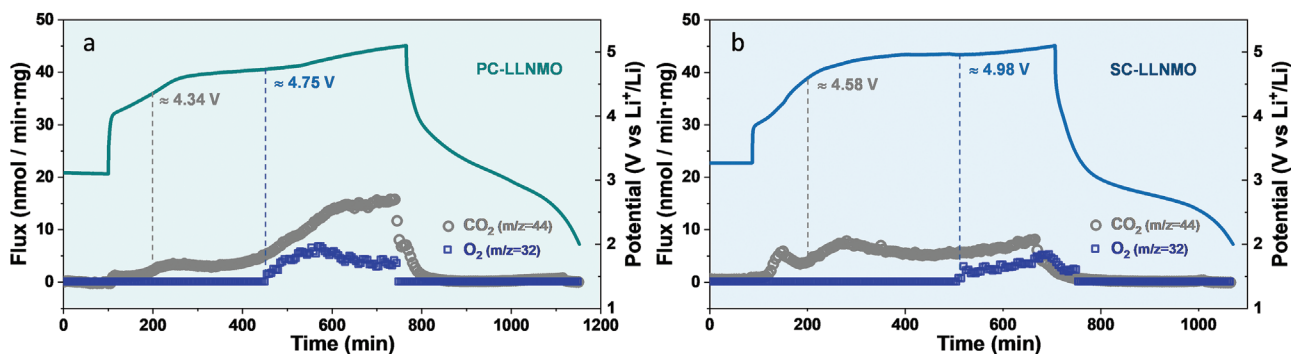


Figure 2. The gas evolution profiles of CO_2 ($m/z = 44$) and O_2 ($m/z = 32$) during the first galvanostatic charge and discharge process of a) PC- b) SC-LLNMO electrodes. The charge and discharge profiles were measured in the potential window from 2.0 to 5.1 V at the current density of 40 mA g⁻¹.

situ GC-MS tests, which is beneficial for obtaining accurate results of O₂ and CO₂ evolutions. The measurements were galvanostatic charge and discharge tested between ≈2.0 and 5.1 V at the current density of 40 mA g⁻¹. Both PC- and SC-LLNMO exhibited the oxygen-related plateau with higher potential than that in coin cells during the first oxygen activation process due to the high current density and polarization caused by in situ GC-MS cell. Massive O₂ can be detected in potential window from 4.7 to 5.1 V in PC sample, whereas the oxygen release started from 4.98 V in SC sample with limited lattice oxygen loss (Figure 2). It proved the morphology control of single-crystal is beneficial to suppress the excessive oxygen oxidation reaction from lattice oxygen to gaseous oxygen, which is fully consistent with electrochemical results.^[16] Moreover, CO₂ evolution can be divided into two regions, in which the first region started from 4.34 V was induced by the decomposition of carbonate impurities such as Li₂CO₃. And the other region started from 4.6 V can be attributed by the electrolyte decompositions caused by nucleophilic attack of superoxo species and/or Ni catalysis on the surface.^[17] Although the CO₂ evolution can be observed in two samples, the SC-LLNMO displayed less CO₂ release benefited from the single-crystal morphology with less specific surface area (Figure S6, Supporting Information). The GC-MS results provided the solid evidence that the design of single-crystal morphology is beneficial for effectively suppressing the CO₂ and O₂ gas release, further guiding the development path of commercial next-generation cathode materials. The ex situ O 1s X-ray photoelectron spectroscopy (XPS) was also performed to track the oxygen behaviors in both PC and SC samples during the initial cycle (Figure S8, Supporting Information). For pristine PC-LLNMO electrode, the peaks of oxygen decomp lattice oxygen (O²⁻) are located at 529.3, 531.1, and 532.9 eV, respectively. After charging to 4.8 V, an obvious peak appeared at 530.6 eV, which can be attributed to the signal of oxidized lattice oxygen (Oⁿ⁻). It disappeared after the first discharging to 2.0 V, suggesting the Oⁿ⁻ was reduced to lattice oxygen. Moreover, the SC-LLNMO electrode displayed the Oⁿ⁻ signal at 530.7 eV after the first charge, and the signal disappeared after discharged to 2 V. The O 1s XPS results proved that anionic oxygen redox reaction can be triggered within PC- and SC-LLNMO samples upon cycling.

To investigate the structure evolution, in situ XRD was conducted to both PC- and SC-LLNMO samples upon delithiation/lithiation processes (Figure 3, Figures S9 and S10, Supporting Information). The peaks of aluminum current collector and conductive agent were clearly marked displayed in Figure S11, Supporting Information. During the first charging process, the (003) peak of layered PC-LLNMO shifted to lower diffraction angle in slope region (≈4.3 V) and further almost kept unchanged in the plateau region (Figure 3a). Meanwhile, the (101) peak shifted to the high diffraction angle at the beginning of first charge and then basically maintained the location in oxygen-related plateau region. The shifts of (101) and (003) peaks accompanied by Li⁺ (de)intercalation processes were related to the evolutions of a and c lattice parameters, respectively. Upon the first charging process, a-lattice parameter decreased first and then kept constant, while the c-lattice parameter increased first and then kept the value. During the subsequent discharging process, the (003) peak gradually shifted to

high diffraction angle, and then moved to low angle at the end of discharging process.^[18] Meanwhile, the (101) peak gradually shifted to low angle upon this process, which indicates c-lattice parameter decreased first and then increased, whereas a-lattice parameter kept decreasing. Upon the second charging process, both (003) and (101) peaks showed the symmetrical changing trend with the first cycle. On the contrary, the (003) and (101) peaks of SC sample displayed the similar trend to the PC sample during the first charging process (Figure 3b). Upon the first discharging process, the c-lattice parameter kept decreasing and the a-lattice parameter increasing, which is totally different from the a/c-lattice evolutions in PC sample, which might be attributed to the differences of the potential oxygen-related plateau and the amount of oxygen release between PC- and SC-LLNMO electrodes. Both a and c-lattice evolutions upon the second cycle possess the reverse tendency with that of the first cycle, which proves the SC-LLNMO harvested the excellent structural reversibility upon cycling. Notably, the superlattice peaks of PC sample in 20–23° can be observed at the beginning of the first charge and gradually disappeared upon subsequent cycles. On the contrary, the superlattice peaks such as (020) and (110) can be well preserved in SC sample during initial two delithiation/lithiation processes. The superlattice peaks can be obviously maintained even after 5 cycles (Figure S12, Supporting Information). It proved Li⁺ ions within TM layer can be well maintained in SC sample upon cycling, whereas the superlattice structure was destroyed in PC sample because of irreversible Li migration induced by serious oxygen loss during the oxygen activation process. These results demonstrated that the morphology control of single-crystal is beneficial for the maintenance of the superlattice structure, which provides a solid foundation to continuously utilize the additional oxygen-related capacity and effectively enhance the structural stability upon long-term cycling. More intriguingly, during the initial two Li⁺ (de)intercalation processes, PC-LLNMO displayed the large volume change of 2.34%, while small ΔV of 1.49% can be achieved in SC-LLNMO (Figure 3), which indicates the layered cathode materials with single-crystal morphology are beneficial for harvesting the excellent structural stability, the limited cracks, and superior electrochemical performances.

Surface-sensitive Raman measurement was conducted to observe fine structure change in both PC and SC-LLNMO cathodes, which was difficult to be detected by XRD measurement (structural information in bulk) (Figure 4a,b). For pristine PC-LLNMO electrode, the peak located at ≈430 cm⁻¹ was generally considered to be related to the monoclinic Li₂MnO₃ phase with C/2m space group, and two peaks at ≈490 and 610 cm⁻¹ could be attributed to the E_g and A_{1g} vibrations, respectively, which belongs to the layered structure with R-3m space group.^[19] Compared with pristine state, the peaks of both E_g and A_{1g} vibrations in PC-LLNMO broadened and appeared an obvious red shift after 100 cycles, which proves the layered structure in PC sample was degraded. Meanwhile, the A_{1g} vibration of C/2m also appeared broadened, which suggests the superlattice structure gradually faded upon cycling, which is consistent with in situ XRD results.^[19] More importantly, an obvious broad peak at 630 cm⁻¹ was observed, which can be attributed to the cubic spinel phase with Fd-3m space group, further resulting in severe voltage decay and inducing the rapid decline of energy

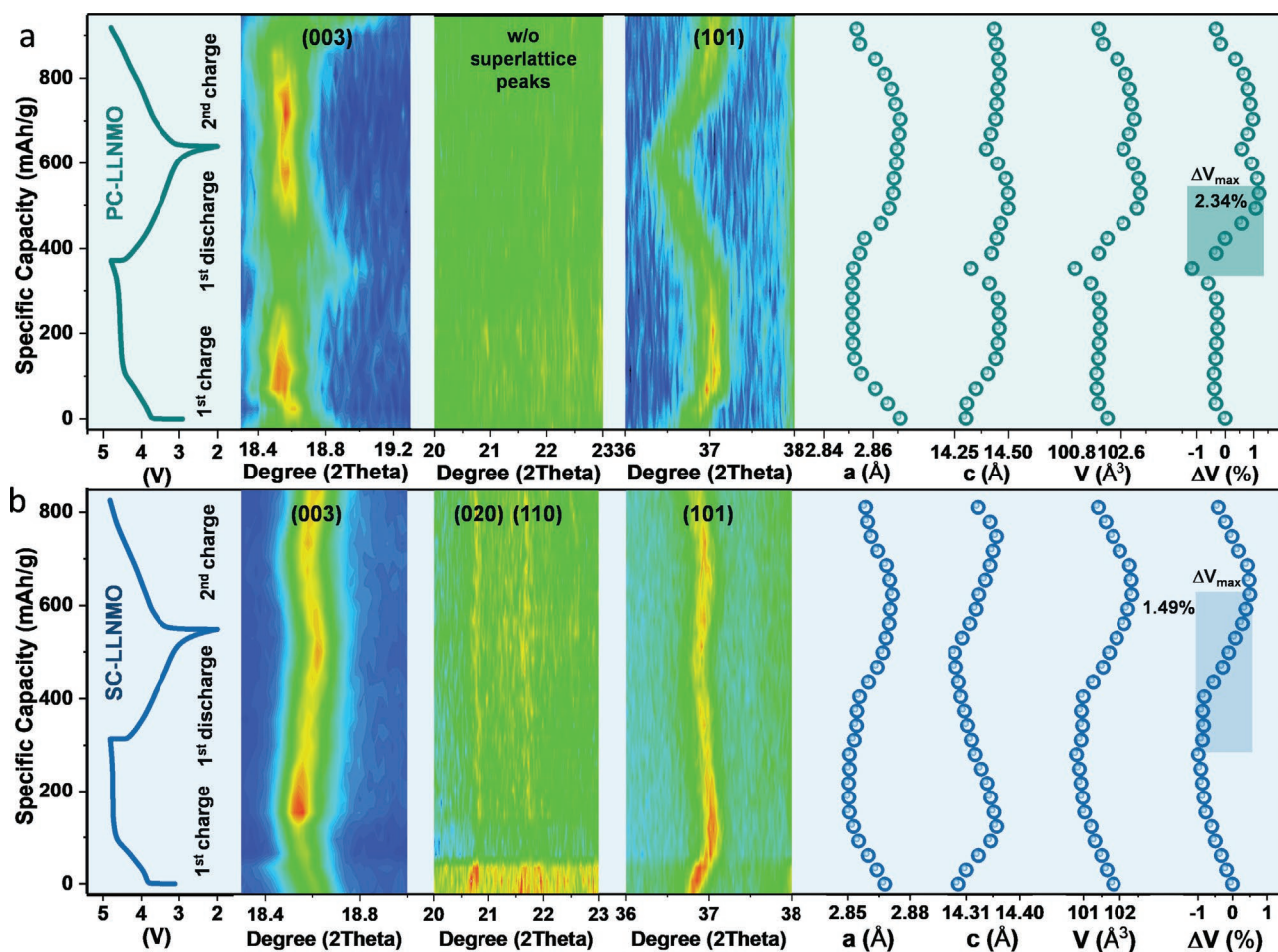


Figure 3. The in situ XRD results of a) PC- b) SC-LLNMO electrodes during the initial two cycles at current density of 15 mA g^{-1} . The potential profiles and corresponding color-coded images of the (003), (104), and superlattice peaks were shown to clearly observe structural evolutions. The Rietveld refined a-lattice, c-lattice parameters, unit cell volume, and volume changes of PC- and SC-LLNMO electrodes were calculated by the GSAS2 software. Besides, the background difference of color-coded images in SC-LLNMO was caused by the accidental beam close at the beginning of the first charge. The X-ray beam restarted immediately, and the intensity of peaks and background recovered to normal state later.

density of battery systems. In contrast, the E_g and A_{1g} vibrations of R-3m as well as the A_{1g} vibration of C/2m space group can be well preserved in SC-LLNMO with absence of the spinel-like signal even after 100 cycles. More importantly, it is worth mentioning that the characteristic of C/2m also can be well maintained after 100 cycles, which is beneficial for the utilization of oxygen redox reactions during long-term cycling.

To obtain direct evidence of structural evolution upon cycling, high-resolution TEM (HR-TEM) observations were performed in both PC and SC samples at pristine state and after 100 cycles (Figure 4c–f). In pristine PC-LLNMO, R-3m and C/2m domain can be clearly observed, which proves the existence of both layered structure and superlattice structure. More intriguingly, obvious spinel phase domain was detected after 100 cycles, displaying the coexistence of the hexagonal R-3m layered structure and Fd-3m spinel structure in secondary particles, which provides the direct evidence of the phase transition from layered to spinel in PC sample. The harmful layered/spinel phase transition would induce the serious voltage decay upon cycling, which greatly decreases the energy density of Li-rich cathode materials and further hinders its practical applications. In

contrast, the R-3m domain was observed in SC sample at both pristine and after 100 cycles, indicating the excellent structural stability can be achieved during long-term cycling. Notably, the C/2m domain also can be well preserved even after 100 cycles, which is beneficial for the sustained utilization of capacity triggered by oxygen redox activities upon cycling. The Selected Area Diffraction (SAED) was performed to further prove that the phase transition from layered to spinel was greatly suppressed in SC-LLNMO upon the cycling (Figure S13, Supporting Information). As a result, PC sample displayed the serious voltage decay of 0.257 V after 50 cycles, whereas the limited voltage fade (0.125 V) can be realized in SC sample at the same electrochemical conditions. These findings including ex situ Raman spectroscopy, HR-TEM images, and electrochemical performance proved that the single-crystal morphology can not only enhance the structural stability but also harvest oxygen-related capacity during long-term cycling.

Moreover, we tracked the morphology change of both PC and SC samples after 100 cycles by SEM (Figure 4g,h). In PC sample, serious crack can be obviously observed, in which primary particles suffered from the destructive crack with the

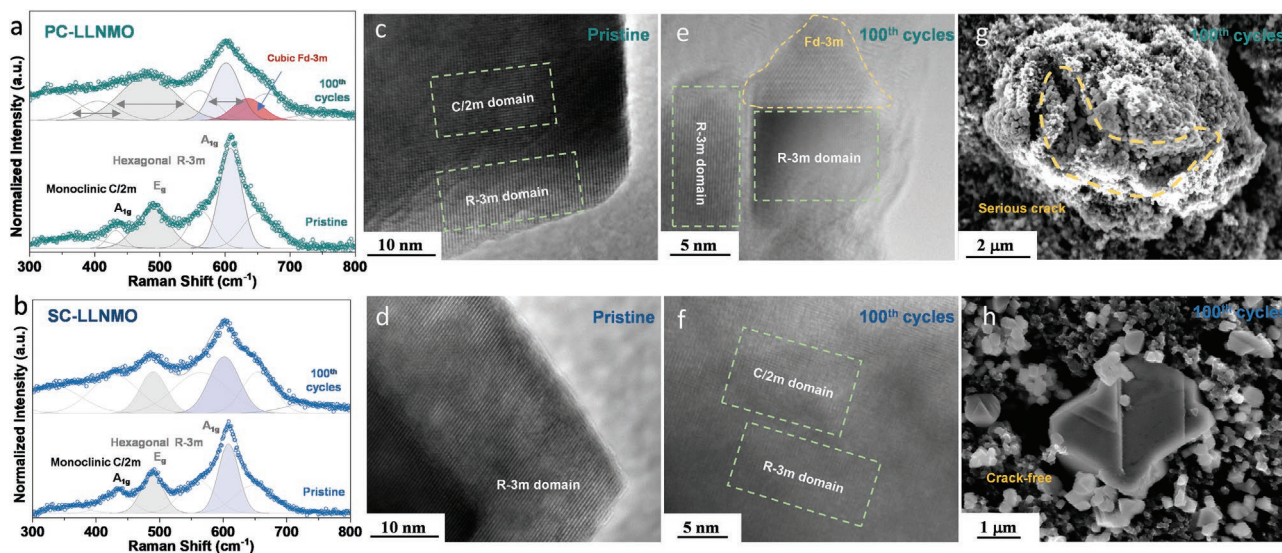


Figure 4. The ex situ Raman spectra of a) PC- b) SC-LLNMO electrodes at the pristine state and after 100 cycles. HR-TEM images of PC-LLNMO c) at the pristine state and e) after 100 cycles. HR-TEM images of SC-LLNMO d) at the pristine state and f) after 100 cycles. SEM images of g) PC- h) SC-LLNMO samples after 100 cycles.

serious exfoliation of secondary particles, which is caused by the anisotropic internal stress. It would inevitably accelerate the area of the interface between electrode and electrolyte, resulting in the serious decomposition electrolyte and structural/electrochemical fade upon cycling. On the contrary, the single-crystal morphology can be well maintained in SC-LLNMO after 100 cycles, delivering the absence of crack and secondary particle generations, which enhances the structural stability and electrochemical performances of Li-rich cathode materials. Therefore, these results effectively demonstrated the morphology design of single-crystal is a promising strategy to optimize and improve the structure stability of Li-rich cathode materials.

3. Conclusion

In summary, the single-crystal Li-rich $\text{Li}_{1.2}\text{Ni}_{0.2}\text{Mn}_{0.6}\text{O}_2$ as cathode material was successfully developed, delivering a novel oxygen-related plateau located at 4.75 V during the first oxygen activation process, different from that of Li-rich oxides with typical polycrystal morphology. After the comprehensive comparisons with polycrystal $\text{Li}_{1.2}\text{Ni}_{0.2}\text{Mn}_{0.6}\text{O}_2$, the serious oxygen release can be effectively restrained within single-crystal electrode, whereas polycrystal sample displayed severe irreversible capacity during the initial cycle. Furthermore, the layered/spinel phase transition only can be well suppressed in single-crystal Li-rich cathode, resulting in the excellent structural stability and limited voltage decay upon long-term cycling. Besides, the limited volume change can be realized in single-crystal morphology upon highly (de)lithiated states, whereas polycrystal sample displayed the serious volume change and induced obvious crack generation upon cycling. By means of these novel features, single-crystal Li-rich cathode achieved the excellent cycling performance in sharp stark with polycrystal counterpart. These findings demonstrated the morphology

design can be regarded as an effectively strategy to realize high-energy-density next-generation Li-ion battery.

Supporting Information

Supporting Information is available from the Wiley Online Library or from the author.

Acknowledgements

This research was partially supported by the National Natural Science Foundation of China (21633003, U1801251). J.S. and X.C. acknowledge the scholarship from the China Scholarship Council (CSC).

Conflict of Interest

The authors declare no conflict of interest.

Author Contributions

J.S. and C.S. contributed equally to this work. J.S., X.C., and H.Z. contributed to the design of the research. J.S. and X.C. performed the experimental data analysis. J.S. conducted the material synthesis, XRD, and SEM measurement. C.S. performed the GC-MS measurements and data analysis. J.S. and X.C. conducted the in situ XRD and spectroscopic characterizations and analysis. P.W. conducted the ICP analysis. H.Y. and Z.C. contributed to the experiment process. X.Y. conducted the TEM analysis. X.C., P.H., and H.Z. supervised the work. All authors co-wrote the manuscript, discussed the results, and commented on the manuscript.

Data Availability Statement

The data that support the findings of this study are available from the corresponding author upon reasonable request.

Keywords

cycle performance, Li-rich cathode materials, oxygen release, single-crystal, structure distortion

Received: October 11, 2021
Revised: November 9, 2021
Published online:

- [1] a) S. Zhao, Z. Guo, K. Yan, S. Wan, F. He, G. Wang, B. Sun, *Energy Storage Mater.* **2020**, *34*, 716; b) M. Sathiyaraj, G. Rousse, K. Ramesha, C. P. Laisa, H. Vezin, M. T. Sougrati, M. L. Doublet, D. Foix, D. Gonbeau, W. Walker, A. S. Prakash, M. Ben Hassine, L. Dupont, J. M. Tarascon, *Nat. Mater.* **2013**, *12*, 827; c) X. Cao, H. Li, Y. Qiao, X. Li, M. Jia, J. Cabana, H. Zhou, *Adv. Energy Mater.* **2020**, *10*, 1903785.
- [2] a) N. Nitta, F. Wu, J. Lee, G. Yushin, *Mater. Today* **2015**, *18*, 252; b) F. Lin, I. M. Markus, D. Nordlund, T. C. Weng, M. D. Asta, H. L. Xin, M. M. Doeff, *Nat. Commun.* **2014**, *5*, 3529; c) J. Lee, D. A. Kitchaev, D. H. Kwon, C. W. Lee, J. K. Papp, Y. S. Liu, Z. Lun, R. J. Clément, T. Shi, B. D. McCloskey, *Nature* **2018**, *556*, 185; d) S. Saha, G. Assat, M. T. Sougrati, D. Foix, H. Li, J. Vergnet, S. Turi, Y. Ha, W. Yang, J. Cabana, G. Rousse, A. M. Abakumov, J.-M. Tarascon, *Nat. Energy* **2019**, *4*, 977.
- [3] a) J. Zheng, P. Xu, M. Gu, J. Xiao, N. Browning, P. Yan, C. Wang, J. Zhang, *Chem. Mater.* **2015**, *27*, 1381; b) J. R. Croy, H. Iddir, K. Gallagher, C. S. Johnson, R. Benedek, M. Balasubramanian, *Phys. Chem. Chem. Phys.* **2015**, *17*, 24382; c) W. Zhang, Y. G. Sun, H. Q. Deng, J. M. Ma, Y. Zeng, Z. Q. Zhu, Z. S. Lv, H. R. Xia, X. Ge, S. K. Cao, Y. Xiao, S. B. Xi, Y. H. Du, A. M. Cao, X. D. Chen, *Adv. Mater.* **2020**, *32*, 2000496.
- [4] a) J. Zhang, Q. Zhang, D. Wong, N. Zhang, G. Ren, L. Gu, C. Schulz, L. He, Y. Yu, X. Liu, *Chem. Mater.* **2021**, *13*, 3071; b) B. Strehle, K. Kleiner, R. Jung, F. Chesneau, M. Mendez, H. A. Gasteiger, M. Piana, *J. Electrochem. Soc.* **2017**, *164*, A400; c) H. J. Yu, Y. G. So, Y. Ren, T. H. Wu, G. C. Guo, R. J. Xiao, J. Lu, H. Li, Y. B. Yang, H. S. Zhou, R. Z. Wang, K. Amine, Y. Ikuhara, *J. Am. Chem. Soc.* **2018**, *140*, 15279.
- [5] a) X. Cao, H. Li, Y. Qiao, M. Jia, X. Li, J. Cabana, H. Zhou, *Adv. Mater.* **2021**, *33*, 2004280; b) D. Eum, B. Kim, S. J. Kim, H. Park, J. Wu, S. P. Cho, G. Yoon, M. H. Lee, S. K. Jung, W. Yang, W. M. Seong, K. Ku, O. Tamwattana, S. K. Park, I. Hwang, K. Kang, *Nat. Mater.* **2020**, *19*, 419.
- [6] E. Zhao, L. He, B. Wang, X. Li, J. Zhang, Y. Wu, J. Chen, S. Zhang, T. Liang, Y. Chen, X. Yu, H. Li, L. Chen, X. Huang, H. Chen, F. Wang, *Energy Storage Mater.* **2019**, *16*, 354.
- [7] a) Y. Liu, J. Harlow, J. Dahn, *J. Electrochem. Soc.* **2020**, *167*, 020512; b) J. E. Harlow, X. Ma, J. Li, E. Logan, Y. Liu, N. Zhang, L. Ma, S. L. Glazier, M. M. E. Cormier, M. Genovese, S. Bouteau, A. Cameron, J. E. Stark, J. Dahn, *J. Electrochem. Soc.* **2019**, *166*, A3031.
- [8] a) E. R. Logan, H. Hebecker, X. Ma, J. Quinn, Y. Hyejeong, S. Kumakura, J. Paulsen, J. Dahn, *J. Electrochem. Soc.* **2020**, *167*, 060530; b) J. Liang, X. Zhang, Y. Zhang, L. Huang, M. Yan, Z. Shen, R. Wen, J. Tang, F. Wang, J. Shi, L. Wan, Y. Guo, *J. Am. Chem. Soc.* **2021**, *143*, 16768.
- [9] Y. Liu, X. Fan, X. Huang, D. Liu, A. Dou, M. Su, D. Chu, *J. Power Sources* **2018**, *403*, 27.
- [10] a) J. Langdon, A. Manthiram, *Energy Storage Mater.* **2021**, *37*, 143; b) Y. Zou, F. Meng, D. Xiao, H. Sheng, W. Chen, X. Meng, Y. Du, L. Gu, J. Shi, Y. Guo, *Nano Energy* **2021**, *87*, 106172.
- [11] a) Y. Xie, J. Yin, X. Chen, X. Liang, Y. Jin, L. Xiang, *ACS Appl. Mater. Interfaces* **2021**, *13*, 3891; b) F. Fu, Y. Yao, H. Wang, G. L. Xu, K. Aminec, S. G. Sun, M. Shao, *Nano Energy* **2017**, *23*, 370.
- [12] J. Hyo, G. Hun, S. Bruno, K. Yang, *J. Power Sources* **2012**, *203*, 115.
- [13] X. Li, Y. Qiao, S. Guo, Z. Xu, H. Zhu, X. Zhang, Y. Yuan, P. He, M. Ishida, H. Zhou, *Adv. Mater.* **2018**, *30*, 1705197.
- [14] a) L. Ye, G. Zeng, K. Nogita, K. Ozawa, M. Hankel, D. J. Searles, L. Z. Wang, *Adv. Funct. Mater.* **2015**, *25*, 7488; b) R. A. House, U. Maitra, M. A. Osorio, J. G. Lozano, L. Jin, J. W. Somerville, L. C. Duda, A. Nag, A. Walters, K. J. Zhou, M. R. Roberts, P. G. Bruce, *Nature* **2020**, *577*, 502.
- [15] a) Y. Wang, E. Wang, X. Zhang, H. Yu, *Energy Fuels* **2021**, *35*, 1918; b) K. Shaju, G. S. Rao, B. Chowdari, *J. Mater. Chem.* **2003**, *13*, 106; c) Z. Shen, L. Cao, C. D. Rahn, C. Y. Wang, *J. Electrochem. Soc.* **2013**, *160*, A1842; d) Y. Zhuang, Y. Bao, W. Zhang, M. Guan, *Chem. Eng. Sci.* **2022**, *247*, 117082; e) M. Lin, J. Cheng, H. Huang, U. Chen, C. Huang, H. Hsieh, J. Lee, J. Chen, W. Su, B. Hwang, *J. Power Sources* **2017**, *359*, 539.
- [16] a) S. Kim, C. Park, S. Hosseini, J. Lampert, Y. Kim, L. Nazar, *Adv. Energy Mater.* **2021**, *11*, 2100552; b) F. Wu, G. T. Kim, T. Diemant, M. Kuenzel, A. R. Schür, X. Gao, B. Qin, D. Alwast, Z. Jusys, R. J. Behm, D. Geiger, U. Kaiser, S. Passerini, *Adv. Energy Mater.* **2020**, *10*, 2001830.
- [17] Z. Zhu, D. Yu, Y. Yang, C. Su, Y. Huang, Y. Dong, I. Waluyo, B. Wang, A. Hunt, X. Yao, J. Lee, W. Xue, J. Li, *Nat. Energy* **2019**, *4*, 1049.
- [18] D. Mohanty, S. Kalnaus, R. A. Meisner, K. J. Rhodes, J. L. Li, E. A. Payzant, D. L. Wood, C. Daniel, *J. Power Sources* **2013**, *229*, 239.
- [19] B. Chen, B. Zhao, J. Zhou, J. Song, Z. Fang, J. Dai, X. Zhu, Y. Sun, *J. Solid State Electrochem.* **2018**, *22*, 2587.